COSY-11

AN INTERNAL EXPERIMENTAL FACILITY FOR THRESHOLD MEASUREMENTS

Collaboration of the COSY–11 Installation

COSY–11
AN INTERNAL EXPERIMENTAL FACILITY FOR THRESHOLD MEASUREMENTS

S.Brauksiepe, D.Grzonka, K.Kilian, W.Oelert, E.Roderburg, M.Rook, T.Sefzick, P.Turek, M.Wolke
U.Bechstedt, J.Dietrich, R.Maier, S.Martin, D.Prasuhn, A.Schnase, H.Schneider, H.Stockhorst, R.Tölle
M.Karnadi, R.Nellen, K.H.Watzlawik
Institut für Kernphysik

K.H.Diart, H.Gutschmidt, M.Jochmann, M.Köhler, R.Reinartz, P.Wüstner, K.Zwoll
Zentrallabor für Elektronik

F.Klehr, H.Stechemesser
Zentralabteilung Technologie,

Forschungszentrum Jülich GmbH, 52425 Jülich, Germany

H.Dombrowski, W.Hamsink, A.Khoukaz, T.Lister, C.Quentmeier, R.Santo, G.Schepers
Institut für Kernphysik, Westfälische Wilhelms–Universität Münster, 48149 Münster, Germany

L.Jarczyk, A.Kozela, J.Majewski, A.Misiak, P.Moskal, J.Smyrski, M.Sokolowski, A.Strzalkowski
Institute of Physics, Jagellonian University of Cracow, 30059 Cracow, Poland

J.Balewski, A.Budzanowski
Institute of Nuclear Physics Cracow, 31342 Cracow, Poland

S.Bowes, A.Hardt
Fachhochschule Jülich, 52428 Jülich, Germany

C.Goodman
Indiana University Cyclotron Facility, Bloomington, IN 47408, USA

U.Seddik
NRC, Atomic Energy Authority, P.O. 13759, Cairo, Egypt

M.Ziolkowski
CERN PPE, 1211 Geneva 23, Switzerland

Abstract

The COSY–11 installation is an internal experiment at the cooler synchrotron and storage ring COSY Jülich. It has been designed for full geometrical acceptance close to threshold for meson production studies, especially in the 1 GeV/c^2 mass range.

The experimental setup makes use of a regular C–type COSY dipole magnet, following a cluster target, to separate reaction products from the beam and to analyze their momenta, thus allowing the observation of charged reaction products at small angles with beam energies close to threshold. Resonances will be identified by missing mass reconstructions from measured four–momenta of two outgoing protons in the predominantly studied $pp \rightarrow ppX$ reaction. In addition, charged mesons either produced directly or from decays of X will be detected.

The different components of the experimental facility are presented.

1 Introduction

Although of fundamental nature, the production of single mesons and mesonic states with and without strangeness in a mass range from the π^0 to the $\Phi(1020)$ meson offers a broad field of unsolved questions in medium energy physics.

This holds especially for the 1 GeV/c^2 region, where the $\Phi(1020)$ is generally believed to be of rather pure s$\bar{\text{s}}$ quark content, whereas the structure of the η'(958) is still being discussed. In case of the scalar mesons $f_0(975)$ and $a_0(980)$ existing data lead to differing interpretations: For instance, a two–quark two–antiquark state, a simple s$\bar{\text{s}}$ nature and a $K\overline{K}$ molecule structure are suggested in case of the f_0 [1–6].

Data of high precision and sufficiently large statistics, in case of small resonances especially in the threshold region, are needed to discriminate between these contradicting interpretations of mesonic states and resonances, which are to be explained on the general basis of QCD.

Threshold meson production necessarily implies vanishing relative momenta of the reaction products leading to extended interaction times. Consequently, final state interaction should be observable for meson–baryon, baryon–baryon and, with at least two mesons being produced, meson–meson systems. Special emphasis should be put on the last–named combination, as, theoretically, two–meson systems represent the simplest objects to study the interaction between hadrons.

The COSY–11 installation might be used for other physics cases as well, and in fact it has been proposed to study the production of a possible πNN dibaryon resonance d' at 2.065 GeV/c^2 via $pp \to d'\pi^+ \to pp\pi^-\pi^+$ in an inclusive measurement at threshold [7].

The proton cooler synchrotron COSY Jülich will provide access to high precision studies covering the mass range described above with proton momenta from 270 MeV/c to $\approx$ 3.4 GeV/c and up to 2×10^{11} stored protons. Using both an electron cooling system for proton momenta $\leq$ 645 MeV/c and stochastic cooling in the momentum range above 1.5 GeV/c high quality beams with a momentum accuracy of Δp/p $\leq 10^{-4}$ and emittances $\varepsilon \leq 1\,\pi$ mm mrad will be available for external as well as internal experiments (section 2).

Early in 1995, the internal COSY–11 experiment has been installed. The experimental setup [8, 9] is shown in fig. 1, including particle tracks resulting from Monte Carlo calculations for the reaction $pp \to ppK^+K^-$ at a beam momentum 1 MeV/c above threshold ($p_{beam}^{thresh} = 3.302$ GeV/c).

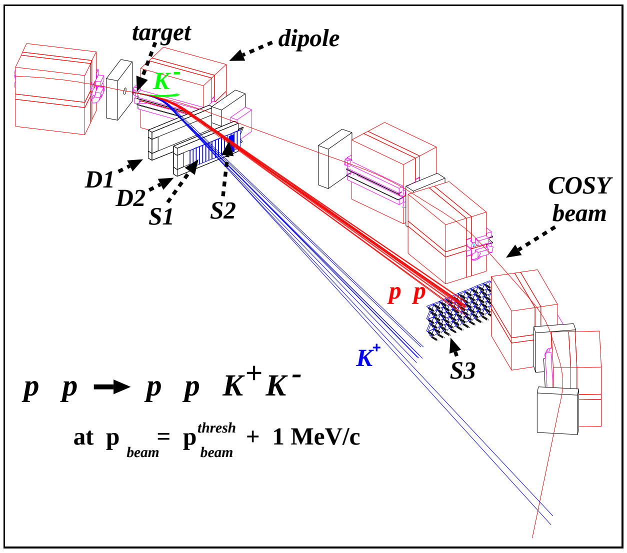

Figure 1: Three-dimensional display of the COSY–11 installation.

A hydrogen cluster target (see section 4) has been installed in front of a normal C–type COSY bending magnet at an internal target location of the cooler synchrotron.

Positively charged reaction products are, due to their smaller momenta, separated from the circulating beam by the magnetic field and diverted towards the center of the storage ring, as indicated in fig. 1. Passing through a specially developed large exit foil of a vacuum chamber, which is mounted inside the dipole gap (section 3), the ejectiles reach the detection system operated in normal atmosphere.

Two stacks of six and eight drift chamber planes respectively (marked D1 and D2 in fig. 1,2, see also section 5), are used to measure the direction of positively charged ejectiles. Thus, including the knowledge of the dipole field, a determination of the particles' momentum vectors is possible.

An arrangement of two scintillation hodoscopes (S1, S2) is used to detect two separate protons in the exit channel. Apart from detecting two protons in two separate hodoscope

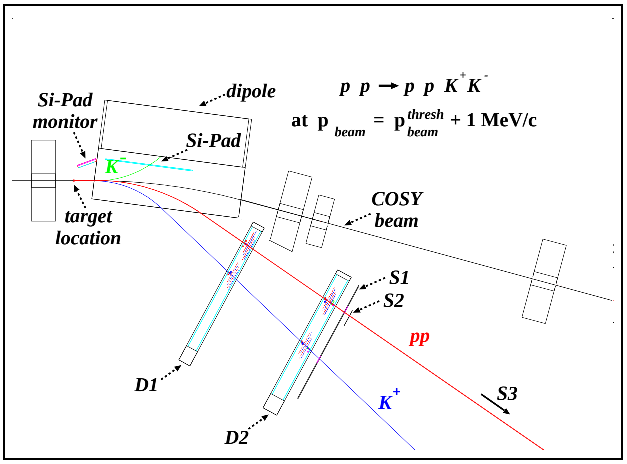

Figure 2: Schematic top view of the detection system close to the target location.

elements, the trigger allows to register two protons with close impact positions in one element via signal amplitude determination (section 6). In addition, positively charged mesons will be detected by the scintillator modules and the drift chamber system. An initial value for the momentum reconstruction of the two outgoing protons in the $pp \to ppX$ reaction is derived from a time–of–flight measurement, started by the S1 scintillation counters. The stop signal is provided by a large area scintillation wall (S3, section 7) spaced by a distance of 9.1 m.

Furthermore, particle identification is possible via this time–of–flight measurement as well as the specific energy loss information dE/dx from the scintillation hodoscopes.

Negatively charged mesons, with their tracks being bent towards the inside of the dipole gap, are detected by an array of silicon pad detectors (section 8) and an additional scintillation counter, both mounted inside the gap (see fig. 2).

A further silicon pad detector system is used to measure recoil protons originating from pp elastic scattering, which allows a normalization to obtain absolute cross sections and a calibration of the detector system.

A missing mass resolution of $< 1\,\mathrm{MeV/c^2}$ for a 1 GeV/c^2 meson or mesonic system X in the $pp \to ppX$ reaction has been estimated from Monte Carlo simulations and is confirmed by first experimental results.

2 Beam Conditions

The special feature of the cooler synchrotron COSY Jülich is its high flexibility in adjusting the tune and choosing optimized beam conditions for each experiment [10]:

The 40 m long straight sections of the ring act as telescopes with phase advance either π or 2π. Each of the arcs is divided in three identical cells with a mirror symmetry in itself. A half–cell has a QF–bend–QD–bend structure with the opportunity of interchanging the focusing–defocusing property. The specific requirement of COSY–11 with its target point TP3 in one of the arcs is a small diameter of the interaction zone:

Simulations show that in particular an uncertainty of the point of interaction in the horizontal plane leads to an increase of the width of the reconstructed mass spectrum [11]. The cluster target beam can be reduced to a diameter in the mm range. Requiring a high luminosity, however, the overlap of both the cluster and the proton beam should be maximum, thus also the expansion of the beam in horizontal direction has to be in the order of the target dimension.

The beam dimensions are defined by the beta–function β, which is due to the focusing strength, i.e. the quadrupole strength, varying with the locality. Thus varying the current of the quadrupoles finally leads to the desired beam dimensions.

Assuming beam particles with a defined momentum ($\frac{\Delta p}{p_0} = 0$) the envelope of the beam at a position s along the ideal orbit depends on $\beta(s)$ and the emittance ϵ, which is constant around the ring. A beam particle with a slightly different momentum ($\frac{\Delta p}{p_0} \neq 0$) performs the same oscillations, however, with respect to an orbit shifted due to the dispersion D at this point. Horizontal and vertical beam dimensions are given by the standard deviations $\sigma_x(s) = \sqrt{\epsilon \cdot \beta_x(s) + D_x^2 \cdot (\frac{\Delta p}{p_0})^2}$ and $\sigma_y(s) = \sqrt{\epsilon \cdot \beta_y(s)}$, respectively.

Notice that at present (without any cooling) at 3.3 GeV/c beam momentum an emittance $\epsilon \approx 1.7\,\mathrm{mm\ mrad}$ and a momentum spread $\delta = (\frac{\Delta p}{p_0}) = 0.7 \cdot 10^{-3}$ are typical. Thus with standard values at TP3 of $\beta_x \approx 11\,\mathrm{m}$ and $D_x \approx 16.9\,\mathrm{m}$ the horizontal enlargement of the beam diameter is mainly caused by the dispersion.

In the calculated "COSY–11 optics" it was attained to constrain the horizontal beam dimension to the width of the cluster target (at present ≈ 9 mm) by minimizing the dispersion at the target point (table 1). For the calculations the program MAD (<u>M</u>ethodical

optics	beam parameters at flat top							
	β_x[m]	β_y[m]	D_x[m]	σ_x[mm]	σ_y[mm]	Q_x	Q_y	γ_{trans}
standard	11.0	10.8	16.9	12.6	4.3	3.57	3.58	-13.9
COSY–11	8.5	14.4	0.2	3.8	4.9	3.68	3.53	2.4

Table 1: Calculated values of beam parameters for the "COSY–11 optics". The actually used optic has a horizontal tune of $Q_x = 3.65$, thus staying below the $\frac{2}{3}$-resonance.

<u>A</u>ccelerator <u>D</u>esign) was used [12]. With the actual setup of the ring as input, the tune, the twist parameters and the quadrupole strength are calculated according to the constraints made by the user. Due to the symmetry of COSY the three families of focusing quadrupoles in the arcs are varied to different values, the three defocusing families are altered the same way.

The tune of the calculated "COSY–11 optics" is only slightly shifted with respect to the "standard optics". As the measurements at COSY–11 are performed only during the flat top, it is possible to reach the new optics by varying the quadrupole strength in the flat top (fig. 3). Injection and acceleration take place with the well known "standard

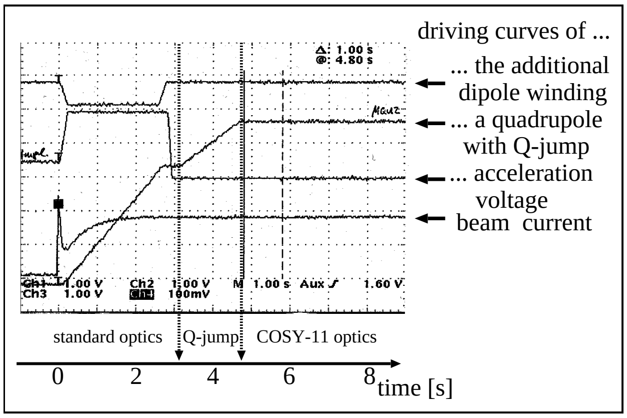

Figure 3: Timing of the COSY cycle. The change of the optics takes place after switching off the acceleration voltage.

optics" always moving γ_{trans} forward. Since the γ_{trans} of the "COSY–11 optics" is too low for the required maximum beam momentum of ≈ 3.4 GeV/c, the beam has to be debunched prior to changing the optics.

3 Vacuum Chamber

The specially designed vacuum chamber is installed inside the gap of a C–type dipole, thus replacing the standard dipole chamber, and is fixed to the magnet in order to support atmospheric forces (fig. 4).

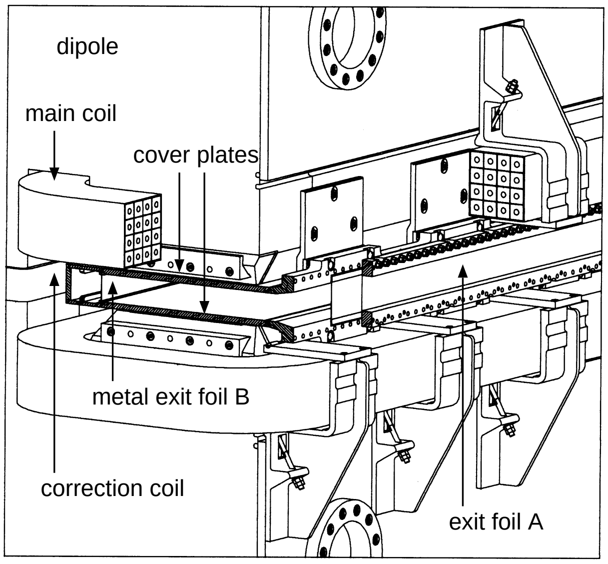

Figure 4: Mounting of the COSY–11 vacuum chamber inside the dipole gap.

The chamber integrates the target point situated in front of the dipole magnet as well as four exit windows, which the ejectiles have to pass towards the different components of the detection system operated in normal atmosphere.

Openings of the chamber (fig. 5) for an ion sputter pump and a titanium sublimation pump in the target region are bridged by high frequency impedance grids.

The exit foil for positively charged ejectiles, protons as well as charged mesons, covers the exit window in longitudinal direction towards the center of the storage ring ('foil A' in fig. 5). For this foil ($1870 \times 76\,\mathrm{mm}^2$) a sandwich arrangement is used. The window is composed of an inward seal, a $30\,\mu$m layer of aluminum foil, and an outward carrier material consisting of two crossed unidirectional sheets of carbon fibers soaked in epoxy resin ($\approx 150\,\mu$m each). Autoclave treatment was used to temper the foil at a temperature of $\approx 130°$ C and a pressure of ≈ 6 bar. Sufficient sealing and clamping effects are achieved by installing the foil between metal flanges with an inserted indium wire ($\emptyset = 2$ mm).

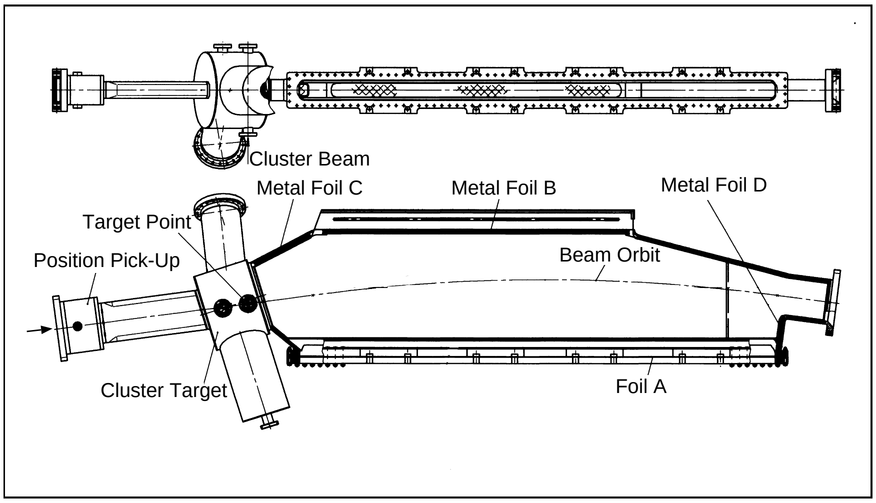

Figure 5: Sectional drawings of the vacuum chamber.

Various tests have shown that, even in case of deliberately cutting the foil with a scalpel after evacuation of the chamber, this type of exit window shows no tendency of being destructed by crack propagation. The choice of materials with low nuclear charge reduces straggling in the exit window to values below the resolution of the detection system.

The three remaining exit windows ('metal foils B, C, D') are made of 150 μm cold–rolled chromium–nickel–steel–foil. At first, in order to avoid shrinkage strains, the metal foils were welded to frames. Thus, after mechanically finishing the frames outside, testing the tightness of welded joints was possible before welding the frames to prepared openings of the chamber. Additionally, the effect of any occuring distortion of the foil is minimized.

At the inside of the dipole gap an exit window covered with 'metal foil B' (dimensions $1140 \times 56\,\mathrm{mm}^2$) is oriented towards the silicon pad detector and the additional scintillation counter for the detection of negatively charged reaction products (section 8). Both detector components are mounted to the chamber as close to the exit window as possible, as indicated in fig. 5. Recoil protons from elastic *pp* scattering leave the chamber crossing 'metal foil C' ($220 \times 46\,\mathrm{mm}^2$) towards a silicon pad monitor detector (see also section 8), which itself is fixed to the vacuum chamber. An additional exit window in the forward direction close to the beam pipe ('metal foil D' in fig. 5) is intended for positively charged particles of larger magnetic rigidity, e. g. deuterons.

Generally, raw materials with small coefficients of permeability ($\mu_R \leq 1.005$), free of pores and inclusions are used.

To achieve mechanical stability, a large thickness (up to 12 mm) was chosen for materials to be welded. Thus, in order to avoid thermal distortion of the different components as well as due to the demand of vanishing gaps on the vacuum side, customary in ultra high vacuum engineering, the common manual tungsten–inert gas welding technique was not applicable in all cases. Instead, laser welding was used for a great number of joints, offering significant advantages due to a concentrated heat input. Striving for high quality welds required frequent cleaning of all parts as well as careful preparation of welded joints. Application of annealing processes at vacuum conditions between the different steps of production removed oxide coatings and, at the same time, reduced inevitable residual stress caused by mechanical processing.

Despite a length of 310 cm, a width of up to 95 cm and a weight of 350 kg, the vacuum chamber meets high standard demands concerning accuracy of dimensions: Deviations in location and inclination of the entry and exit flanges are restricted to few tenths of a millimeter. Limited free space of $< 0.5\,\mathrm{mm}$ between the magnetic poles and the cover plates resulted in tolerance ranges many times over typical values of welded constructions. Thus, after mechanical completion, critical dimensions of the vacuum chamber were checked on a horizontal drilling machine.

By means of an integral helium leak test a helium leak rate of $\leq 1 \times 10^{-9}\,\mathrm{mbar\,l/s}$ was confirmed. Residual gas spectroscopy at a total pressure of $2 \times 10^{-9}\,\mathrm{mbar}$ proved the recipient to be free of hydrocarbon with partial pressures for atomic mass numbers 15 as well as 29 to 100 (except for mass numbers 40 and 44) of $< 5 \times 10^{-13}\,\mathrm{mbar}$ each.

Calculations according to the finite element method accompanying the construction of the vacuum chamber and tests on its load capacity, together with fixed geometrical and physical limiting conditions lead to the shape of the chamber. Cover plates thicker than those used for the other 23 COSY dipoles and solid flanges result in a different response of this special construction to eddy currents. Thus, the dynamical behavior of dipole, quadrupole and sextupole fields differs significantly. A compensation of these effects, which are negligible at high momenta but, with a $\approx 5\%$ change of the dipole field, important at the injection energy, could be achieved by activating a correction coil and by changing the ramping curve of some optical elements of the accelerator.

4 Cluster Target

Interactions of the circulating beam occur on an internal cluster target shown in fig. 6, with the cluster beam source in the lower part and the beam dump in the upper part.

While the pre–cooled target gas passes a laval nozzle, condensation starts under appropriate conditions and clusters of hydrogen with about 10^6 molecular weight grow. The gas is peeled off the cluster beam by the skimmer and the remaining target beam travels through the vacuum system as a homogeneous beam with a small angular divergence ($< 1°$), given by the geometry: It passes two collimators, crosses the scattering chamber and reaches the three–stage beam catcher. Since the highest pressure occurs in the skimmer and the last catcher stage, pumping parallel to the cluster beam is necessary to maintain UHV conditions in the scattering chamber.

At a large distance from the nozzle, the differential pumping stages become ineffective due to increasing conductances between each stage as a consequence of the cluster beam broadening. Because of severe space constraints, special cryopumps were developed in which vacuum chamber and pump are combined in one unit. These cryopumps are equipped with an array of charcoal coated cold sheets where the cluster beam is directed through.

The cluster beam diagnostic is achieved by elastic electron scattering with a 5 keV electron beam: A movable arm, which carries the complete diagnostic system, an electron gun, an electrostatic spectrometer including a Faraday–cup and a channeltron for the detection, allows to scan the target region (fig. 7). The production of hydrogen clusters is shown by the density profile in fig. 8, which was measured 1.4 m behind the nozzle

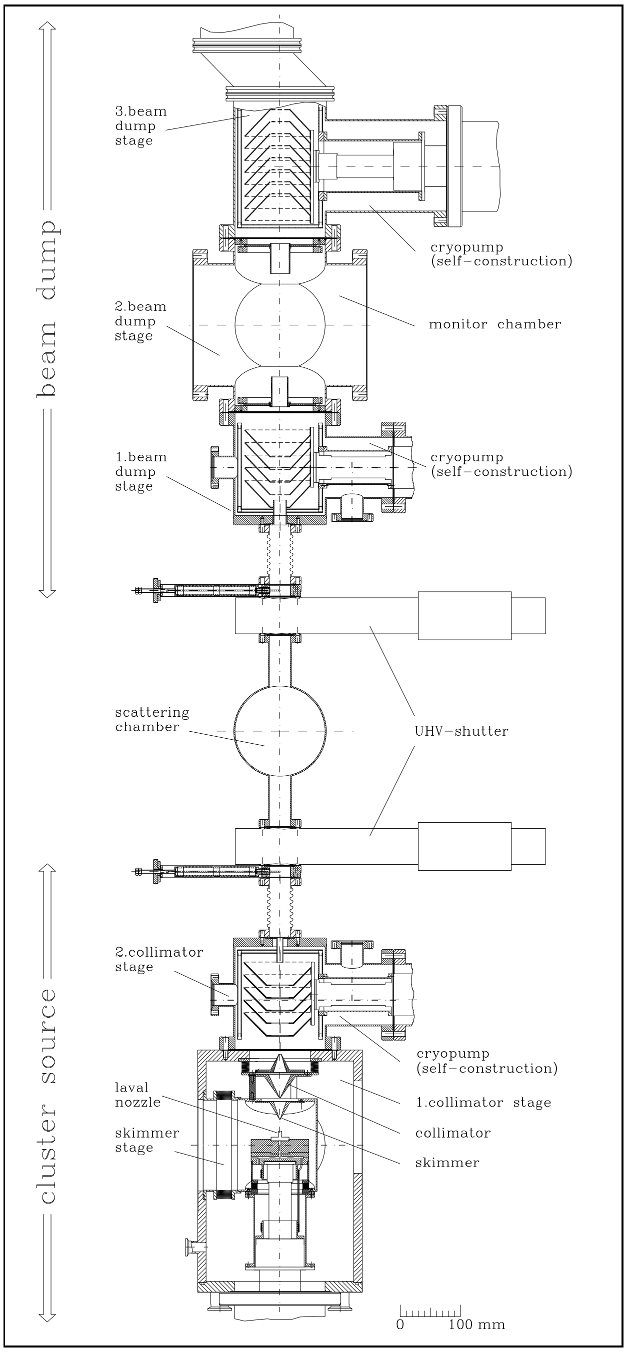

Figure 6: Basic setup of the cluster target for the COSY–11 experiment.

with this monitor system. The areal density as a function of the position arises from a rectangular volume density distribution, which is homogeneous. The measured curve fits very well to such a homogeneous cluster beam with a diameter of $\approx 19.5\,\mathrm{mm}$, thus, resulting from the divergence of the beam, in the scattering chamber a target diameter

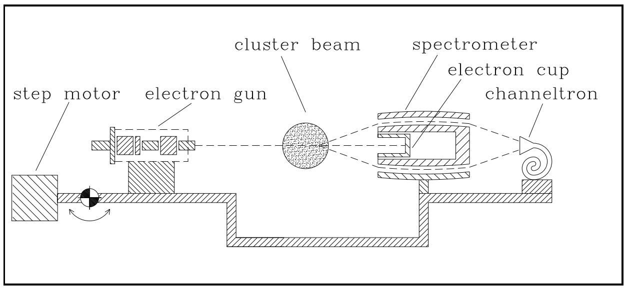

Figure 7: Sketch of the electron scattering diagnostic system.

of ≈ 9 mm is expected. As the target diameter scales with the size of the collimator, the cluster beam width can be varied by use of different collimators. Evaluations of

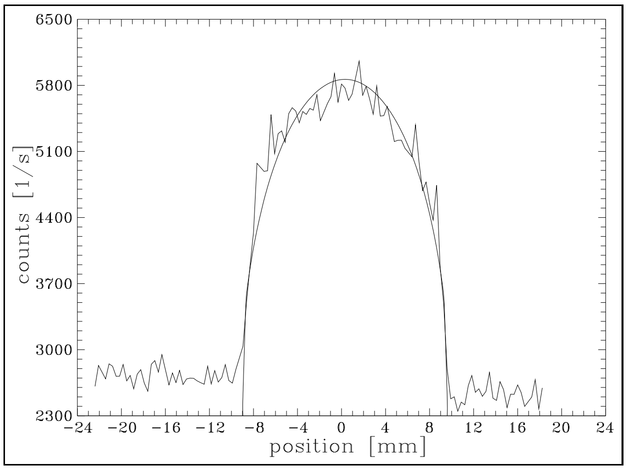

Figure 8: Profile of a cluster beam measured by the monitor system. The solid line is a fit by a profile for a homogeneous cluster beam with a diameter of 19.5 mm. The high background level results from the primary electron beam, like backscattered electrons from the cup.

scattering experiments with a 400 keV α–beam result in a cluster density value of $2.5 \cdot 10^{13}$ atoms/cm^3 for a target diameter of 9 mm in the scattering chamber. The parameters in these tests were: nozzle diameter $d = 18\,\mu$m, nozzle temperature $T = 50\,$K and hydrogen input pressure $p \approx 18\,$bar.

The complete system can be controlled manually or completely automatically via an IEEE–488 bus by a VME system. A more detailed description of the target will be given in a separate publication [13].

5 Drift Chambers

Trajectories of both protons and positively charged mesons are measured with two planar drift chamber stacks [14, 15] spaced by 70 cm and containing together 14 (= 6 + 8) detection planes [16]. The active area of the chambers is 1680 mm wide and 433 mm high. The chamber stack standing closer to the bending magnet contains six detection planes: two planes with vertical wires, two with wires inclined by $+31°$ and two with wires inclined by $-31°$ (see fig. 9). The wires in consecutive planes of each pair are

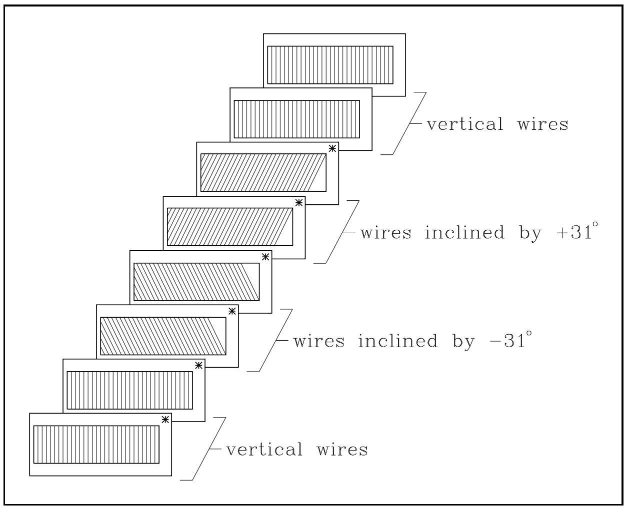

Figure 9: Orientation of wires in the drift chamber containing eight detection planes. The second chamber contains six planes which are indicated by asterisks.

staggered by half of the cell width in order to resolve the left–right position ambiguity with respect to the sense wire. The chosen configuration of detection planes allows to measure the horizontal and vertical coordinates and enables a unique identification of multihit events. It has some redundancy which improves the detection efficiency and ensures some safety in the case when one of the planes breaks down. The same configuration of detection planes was used in the second chamber stack, with this stack being supplemented by two additional planes with vertical wires in order to improve the position resolution in the horizontal direction.

The drift cells are of the graded field type with a width of 40 mm. The cell structure is shown in fig. 10. The indicated voltages are those used in standard operation of the

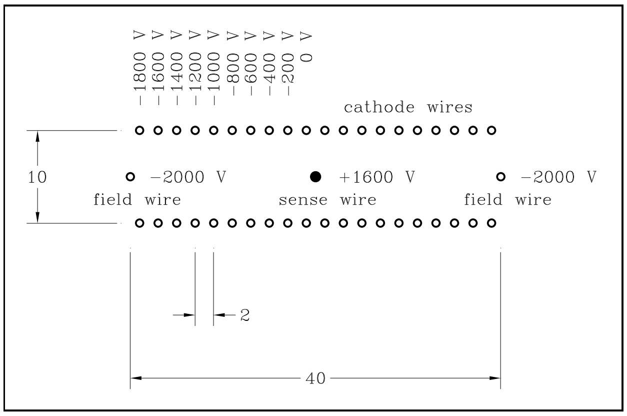

Figure 10: Cell structure and voltage distribution.

chambers with a gas mixture of 50% argon and 50% ethane at atmospheric pressure. The sense wires are made of 20 μm thick gold–plated tungsten, whereas, for the field wires and the cathode wires 50 μm Cu–Be was used.

Each detection plane is built of three frames made of epoxy–fiberglass [17] with glued printed boards for soldering the wires. One frame contains the alternately ordered sense and field wires. On both sides of it there are two frames with the cathode wires. The spacing of consecutive planes is 18 mm.

In case of the near–threshold production of light mesons like π^0 or η the scattered protons share most of the beam momentum and are bent only slightly outside the beam line by the dipole magnet. In order to measure their trajectories, the drift chambers are placed close to the beam pipe. For this reason, one side of the chamber frames is minimized to only 55 mm width. Additionally, in order to avoid a triangular dead area which occurs when inclined wires are stretched only between the upper and lower part of the frames, the wires are attached also to the narrow part of the frames (see fig. 9).

Each of the detection planes is equipped with three 16–channel preamplifier–discriminator cards [18]. The drift time is measured using multihit FASTBUS TDCs (see section 9) in common stop mode with the pulses from the discriminators as start signals and the trigger pulse as the common stop. In the predominant case of particle tracks oriented almost perpendicularly to the detection planes, the maximum drift time corresponding to the maximum drift path of 20 mm is 400 ns. The position resolution for each detection plane is 100 μm (rms), as measured with 1 GeV/c protons.

The particle trajectories are reconstructed using a computer code "MEDUZA" [19]. The code allows for reconstruction of multiple track events. The procedure works properly even if some of the planes don't fire or if additional noise signals occur. The reconstruction efficiency for the set of our chambers is very close to 100%. The particle trajectories determined this way are traced through the magnetic field of the dipole back to the target. Thus it is possible to determine the momentum vectors of ejectiles at the target location. The measurement of the momentum vectors of both emitted protons in the reaction $pp \to ppX$ combined with the information about beam energy allows to compute the missing mass of the produced meson X. In a first measurement on η production at threshold, which was performed with still uncooled COSY beam, a missing mass resolution of about 2 MeV has been obtained.

6 Scintillator Hodoscopes S1 and S2

The scintillation hodoscope S1 consists of sixteen scintillation modules with dimensions of $450 \times 100 \times 4$ mm^3 (Bicron BC 404 [20]). The scintillator elements are arranged vertically and read out at both sides by photomultipliers Thorn Emi 9954B [21]. For minimum ionizing particles a time resolution between 160 ps and 220 ps (rms) has been measured, depending on the impact position. The trigger condition for the predominantly studied $pp \to ppX$ reaction arises from the detection of two protons in the exit channel. Thus, a trigger signal is generated in case of two separate modules of the hodoscope responding. Closer proton tracks hitting the same S1 module, as they are to be expected e. g. for measurements at beam momenta just above threshold, are resolved by a second, movable sixteen elements scintillator hodoscope S2 with module dimensions of $450 \times 13.5 \times 2$ mm^3 (Bicron BC 404 [20], photomultipliers Hamamatsu R 1635–02 [22]).

In case of even closer proton trajectories, a detection of two protons in one module of either hodoscope via signal amplitude is implemented: As the pulse height sum of the upper and lower readout component of a single hodoscope module proves to be approximately independent of the particle's impact position [23, 24], a fast pulse integrator unit with 8×2 inputs has been realized in SMD technique as a standard single–width NIM–module [25]. A block diagram is shown in the upper part of fig. 11, in the lower part the principle is illustrated by examples of output signals resulting from different idealized inputs. For an input pulse of more than 4 ns width and signal amplitudes up to -5 V two

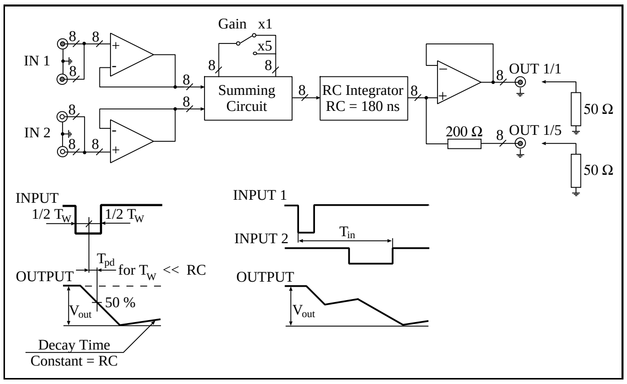

Figure 11: Integrator block diagram.

output signals are available: Apart from a one–to–one output (≤ -5 V into 50 Ω load, OUT 1/1) an additional attenuated output with a maximum -1 V into 50 Ω is provided (OUT 1/5). With rise times corresponding to the integration and a propagation delay of $T_{pd} < 2$ ns a decay time constant of 180 ns was chosen for the integrated output signal. An overall gain of $\times 1$ or $\times 5$ may be selected via on–board jumper settings.

7 Scintillator Wall S3

The stop signal for the time–of–flight measurement is generated by a large area scintillation wall (S3), which has been constructed according to the idea of the AMADEUS detector developed at the University of Bonn [26, 27].

A sketch of the detector principle is shown in the upper part of fig. 12: An impinging charged particle causes the production of scintillation light along its path through a non–segmented scintillation wall with dimensions of 220 cm horizontally, 100 cm vertically and a thickness of 5 cm (Bicron BC 404 [20]). The emitted scintillation light is viewed by a matrix arrangement of 217 photomultipliers (Thorn Emi 9954B [21]) with a 4 cm air

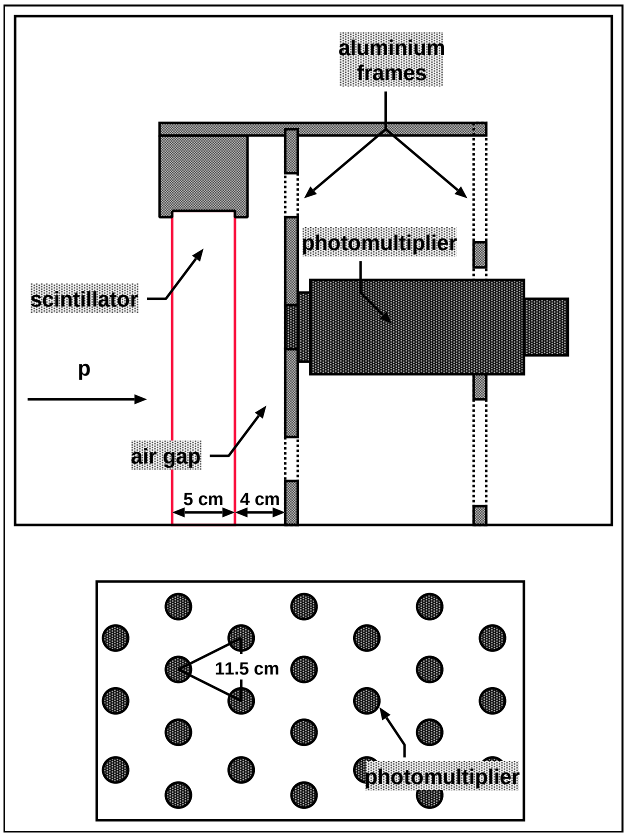

Figure 12: Principle of the S3 scintillation wall (upper part) and schematic view of the photomultiplier matrix (lower part).

gap separating scintillator and photomultiplier matrix. The phototubes occupy the edges of equilateral triangles of 11.5 cm as indicated in the lower part of fig. 12. Due to total reflection at the transition between scintillator material and the air gap, the amount of light registered by each photomultiplier drops off rapidly with increasing distance to the particle's impact position. Thus, only a few photomultipliers within a certain cone show a considerable response to the particle passing through. Consequently, the energy deposition of the particle can be derived from the pulse height sum seen by these participating photomultipliers, while the center of gravity of the pulse height distribution allows the determination of the particle impact position. Besides, the restriction of few photomultipliers responding implies the possibility of separating two or more close impact positions.

The detector concept results in an intrinsically optimized timing information: With conventional scintillation detector arrangements, the light pulse is spread out timewise because of multiple total reflection along its path through scintillator material and light–guide. However, with the presented detector setup, only direct light is detected by the phototubes: Once totally reflected, light is absorbed by the black painted edges of the scintillator wall.

Test measurements with minimum ionizing particles result in an intrinsic time resolution between 135 and 190 ps (rms), depending on the impact position relative to the photomultiplier triangle. Therefore, an overall resolution for the time–of–flight measurement between start (S1) and stop detector (S3) in case of protons with a typical momentum of 1 GeV/c in the range of 195 ps up to 265 ps (rms) is expected, which leads to an accuracy of $\Delta p/p \approx 1-1.5\,\%$ for the determination of the proton momentum.

Despite its optimization in view of timing accuracy, a position resolution of ≈ 1.0 cm (rms) is achieved for these typical momenta with the described geometrical parameters of the detector.

Leading–Edge–Discriminator Module

With regard to the large number of photomultiplier channels, a sixteen channel leading–edge discriminator (LED) module has been designed for different COSY experiments and is used for S3 signals at the COSY–11 installation. Beside electrical properties like small time walk, a large dynamic signal range, and a short input–to–output delay time the module price has been optimized during the development. The discriminator is placed in a slightly modified eurocard mechanic instead of using a standardized but expensive bus system, like CAMAC or FASTBUS. Nevertheless, to secure compatibility to other hardware components used at COSY, the discriminator crate provides a VICbus (ISO/IEC 26.11458) interface [28,29], the desired standardized cable bus for the COSY–11 data acquisition system, and an RS232 serial interface.

The block diagram of one channel of the discriminator module is shown in figure 13. Basically, the discriminator consists of the RAL10 chip, an integrated timing discrimi-

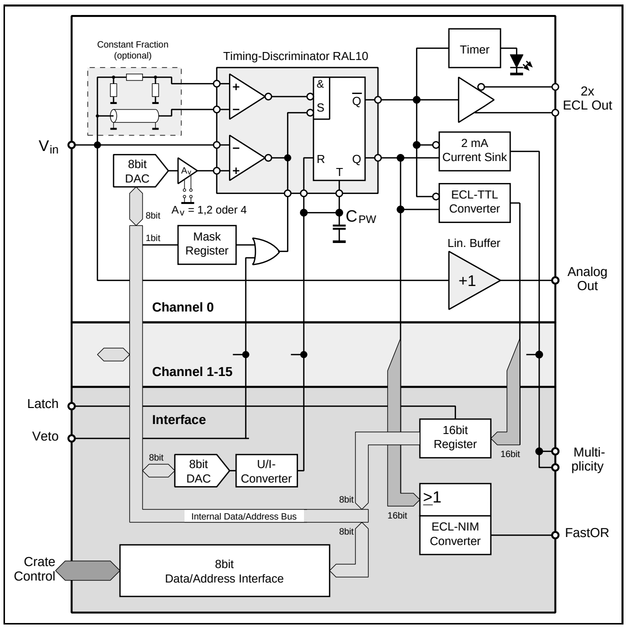

Figure 13: Block diagram for one channel of the new developed leading–edge–discriminator module.

nator designed at the Rutherford Appleton Laboratory (UK) [30,31]. This commercially available IC is chosen because of its good timing properties in combination with fast photomultiplier signals and the fact, that it contains all the electronic building blocks needed to realize an LED as well as a constant–fraction discriminator at a minimum of additional hardware. Moreover, each discriminator channel consists of an 8–bit DAC for threshold adjustment with selectable range and resolution, a mask register to enable/disable the channel, an ECL twisted–pair line driver, and a linear buffer amplifier (gain = +1) to generate the ADC input signal instead of using a power divider to split the photomultiplier signal. Beside one 8–bit DAC to control the output pulse width of all sixteen channels (5 ns to 300 ns) the LED module has a fast ECL wired OR output for multiplicity. Via VETO and SYNC, two additional digital inputs using NIM level, the discriminator can be controlled during the measurement.

First use of the new LED module has demonstrated good results meeting the desired specifications. Regarding the discriminator speed a counting rate of 100 MHz and a double pulse resolution of 8 ns could be achieved. The input–to–output delay of the module amounts to 11.5 ns with a delay matching better than 0.4 ns. For an amplitude range exceeding 30:1 an intrinsic time walk of less than 800 ps has been attained for signal risetimes between 1 ns and 5 ns. In combination with a measured timing jitter of less than 150 ps for an amplitude range of -10 mV to -2 V and signal risetimes as mentioned above the LED provides an entirely adequate time resolution for the experiment.

8 Silicon–Pad Detector

For the detection of negatively charged mesons, which are diverted towards the yoke of the COSY C–type bending magnet, a silicon pad detector has been developed for operation inside the dipole gap (fig. 2, 5). An additional silicon pad monitor detector is used to detect recoil protons from *pp* elastic scattering for the normalization of cross sections and the calibration of the detection system.

Both silicon pad detectors [32] consist of identical elements containing four separate pads (fig. 14) corresponding to a design of the PS 202 (JETSET) experiment [33], thus providing a granularity of about 5 mm horizontally and 20 mm vertically. Front–end

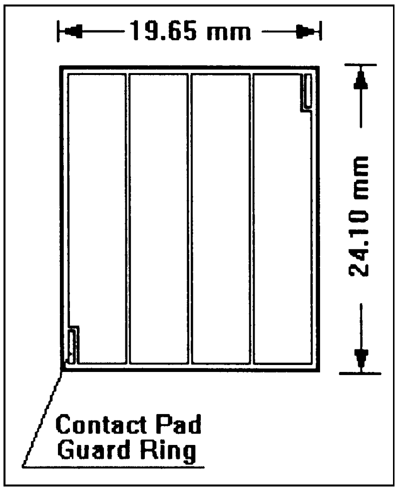

Figure 14: Silicon pad chip.

electronics for the readout of these 864 pads altogether are made up of the AMPLEX–16 chip developed at CERN [34]. The readout of the AMPLEX chip is carried out by means of the CAMAC modules DRAMS Receiver and DRAMS Control [35,36]. In parallel two groups of up to 512 pads each are read out sequentially, digitized and added to the event data.

Geometrical conditions inside the magnet gap allow for a mechanical construction of the detector consisting of three rows of vertically arranged silicon chips one above the other. As the guard ring area of the detector elements (fig. 14) is insensitive concerning particle detection, a sufficient overlap of the individual chips is to be preferred. From the need of exchanging single detector elements in case of defect, a *Detector Module* with overlapping detector elements has been designed (see fig. 15). The assembly of

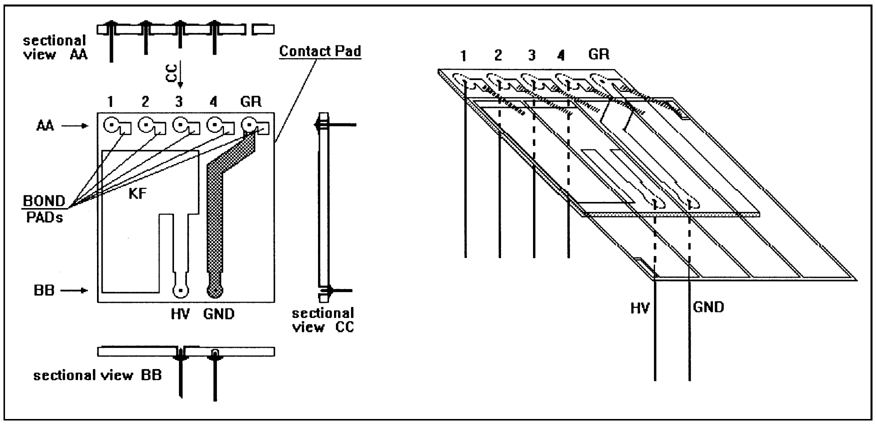

Figure 15: Silicon Pad Detector Module.

single *Detector Modules* on appropriately prepared areas on the detector board forms the complete detector with the individual areas being slightly inclined to provide an optimum overlap of the detector elements.

According to the geometry of the mechanical construction, a printed circuit board has been developed for the readout of three AMPLEX–16–chips covering 48 channels (*AMPLEX–Board*), which is to be mounted on the back of the detector–boards.

Because of large distances (25 - 100 m) between the front–end electronics and standardized CAMAC/NIM readout, there is a danger of control signals for the readout of AMPLEX–chips being transmitted defectively. To avoid such effects, a *CONTROL–Board* for front–end operation of three *AMPLEX–Boards* has been designed. Thus, control signals necessary for the readout of AMPLEX–chips are generated directly at the front–end, and, in addition, driver electronics are provided for the transmission of analog signals from the silicon detectors to CAMAC/NIM readout electronics.

The readout of an event is started by the experiment trigger signal. In order to derive control signals required for the readout and to optimize the readout timing, an *Event–Control–Module* is used, which allows for a simple adjustment of readout timing in case of timing changes in the main event trigger. Additionally, control signals from the DRAMS–Control–Module are regenerated and shaped for supplying the front–end CONTROL–Board with the necessary signals.

When operating the silicon pad detector, the temperature at the front–end electronics situated inside the dipole gap is directly related to the duration of the COSY accelerator cycles. With cycles of 6–12 s the temperature at the electronics rises up to 40° C. As data taking is restricted to the flat top, one tends to use longer machine cycles: After several hours of operation with cycles of 60 s a temperature of 32° C was measured at front–end electronics.

9 Data Acquisition

At COSY–11, a general data acquisition system is used, which has been developed for several experiments at COSY. It's architecture is based on available standards [37].

CAMAC, FASTBUS and VME are used at the front–end as digitizing and auxiliary systems. Readout and event building are performed by a multiprocessor arrangement of intelligent CAMAC controllers, FASTBUS masters and VME CPUs, as shown in fig. 16.

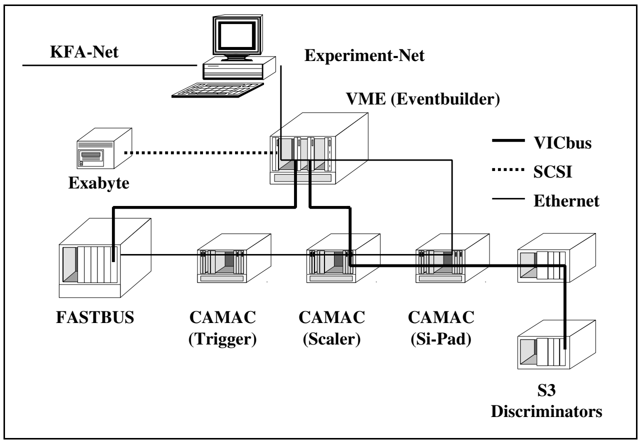

Figure 16: Schematic overview of the architecture of the data acquisition system.

For the flow of event data the VICbus ISO/IEC 26.11458 [28,29] has been adopted as standardized intercrate and workstation connection. Due to its widespread use and rich functionality OS–9 has been chosen for the intelligent front–end devices. As experiment workstation a DEC Alpha with OSF/1 is used.

The experiment makes use of a FASTBUS crate equipped with LeCroy ADC 1881 and TDC 1875A for the scintillator signals and the multihit TDC 1877 and TDC 1879 modules for the drift chamber data. The front–end hardware consists of this FASTBUS crate and three CAMAC crates with their own intelligent controllers, Struck STR 330 [39] and CES VCC2117 and VCC2118 [40] respectively. As subeventreader we use two Eltec E6 [41]. The VSB interfaces serve as ports to the VICbus via a special module [37]. The eventbuilder (CES FIC8234 [42]) resides in the same VME crate as the subeventreaders and is responsible for data recording on EXABYTE 8505 [43] tape. Additionally, the eventbuilder can send a stream of sample events to the workstation via TCP. All front–end and eventbuilder CPUs are diskless, the experiment workstation acts as server for NFS, BOOTP and TFTP.

For event synchronization a system developed by GSI Darmstadt is used [44]. The experiment control software is distributed over several processors. In general it is realized as front–end realtime software implemented on the controller boards in CAMAC, FASTBUS and VME (servers) and the man/machine–interface part running on the workstation (one or more clients). The front–end software with its communication to the workstation is designed according to a client server connectivity model and an object oriented approach. The concept of the software is logically based on MAP/MMS (Manufacturing Message Specification, ISO 9506 [45]). MMS, an application layer protocol, aids communication among distributed programmable manufacturing devices. With MMS being a quite complex tool, it was decided to use some of the benefits instead of its full complexity: As being dedicated to physical experiments, our solution is called Experimental Message Specification (EMS). All peripherals like CAMAC, FASTBUS and VME with their intelligent devices act as servers for the client workstation. Each server is built around an abstract object, the Virtual Experimental Device (VED). All VEDs contain a set of objects that help accessing the functionality represented by e. g. instrumentation systems like a group of FASTBUS ADCs, auxiliary systems (e. g. scalers) or simple variables. To manipulate these objects EMS provides a set of generic services. For the transport system TCP/IP is used, offered by nearly all operating systems known in the physical experimental field.

On the workstation side, the experiment control client software consists of various control processes with a user interface [46] realized in OSF/Motif and communication with the front–end realtime system realized by the EMS. Thus, experiment handling, covering experiment preparation, run control with data taking and tape handling as well as online data analysis from the distributed event flow, is provided in a user–friendly way. The online analysis, e. g. histograms of assigned detector channels, hit pattern distributions of detectors and an online event display make use of established software standards, e. g. PAW, HPLOT, HBOOK [47] of CERN software.

10 Geometrical Acceptance

The geometrical acceptance of the COSY–11 detection system is limited especially in the vertical direction due to the narrow opening of the dipole gap with an internal height of 60 mm. Fig. 17 shows the geometrical efficiency derived from Monte Carlo calculations, i. e. the ratio of detected events to the number of generated events, as a function of the beam momentum above threshold and the excess energy, respectively, for the reaction $pp \rightarrow ppK^+K^-$.

With the experimental technique consisting of determining the invariant mass of the produced meson or mesonic system via measuring the four–momenta of both protons in the exit channel, the minimum requirement for a detected event is defined by a double proton hit in the drift chamber system. Further information, with limited acceptance, is obtained by the detection of outgoing positively and negatively charged mesons via hits in the drift chambers and the silicon pad detection system, respectively. Geometrical

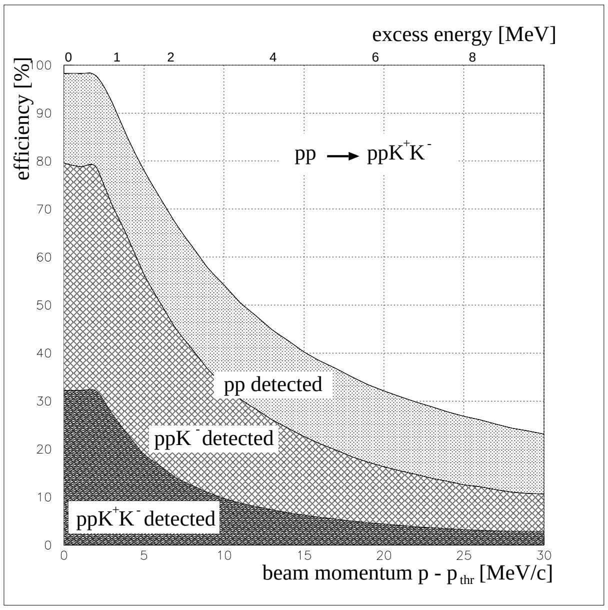

Figure 17: Geometrical efficiency of the detection system for the reaction $pp \to ppK^+K^-$.

efficiencies for detecting two protons and, in addition, the negatively charged kaon as well as for detecting two protons and both charged kaons are plotted. The decay of the kaons is taken into account.

Up to excess energies of ≈ 0.8 MeV above threshold full geometrical acceptance for the detection of two protons is obtained, while the efficiency for detecting an additional charged kaon reaches $\approx 80\,\%$. With increasing kinetic energy in the two proton system the protons become more likely to hit the dipole iron and, consequently, the ratio for detecting two protons drops off to $\approx 25\,\%$ at an energy of 10 MeV above threshold. At this energy, the corresponding detection efficiencies for three and four charged particles in the exit channel decrease to a level of $\approx 10\,\%$ and $\approx 3\,\%$, respectively.

Conclusion

The experimental setup of the internal experiment COSY–11 at the cooler synchrotron COSY Jülich has been presented. Physics at this installation will focus on the study of rather narrow states close to threshold.

The experimental approach bases on the missing mass technique, i. e. the analysis of mesonic reaction products is founded on the measurement of the four–momentum vectors of the outgoing baryons in the predominantly studied $pp \rightarrow ppX$ reaction. A momentum analysis obtained from an accelerator bending magnet in combination with a drift chamber system is supported by a time–of–flight measurement. A supplementary analysis of positively and negatively charged mesonic ejectiles via the drift chamber system or the silicon pad arrangement inside the dipole gap respectively, completes the experimental setup. The experimental facility has been installed and first data taking is in progress. Its detailed description should invite scientists to make use of this recent tool in medium energy physics for new experimental ideas.

Acknowledgements

The design, construction and installation of the presented COSY–11 facility would not have been possible without the help and advice of many people and institutions. We are grateful and appreciate the support very much. For funding our project we would like to thank especially BMBF Bundesministerium für Bildung, Wissenschaft, Forschung und Technologie, the German–Polish Foundation, the State Committee for Scientific Research of Poland and the KFA Jülich. There are too many people we have to and we would like to thank. They all helped us with numerous personal engagements. Thank you to all of them.

References

[1] R.Jaffe, Phys. Rev. D 15 (1977) 267.

[2] K.Au et al., Phys. Lett. 167 B (1986) 229.

[3] D.Lohse, J.W.Durso, K.Holinde, J.Speth, Phys. Lett. 234 B (1990) 235.

[4] J.Weinstein, N.Isgur, Phys. Rev. D 41 (1990) 2236.

[5] D.Morgan, M.R.Pennington, Phys. Lett. 258 B (1991) 444.

[6] R.J.Apsimon et al., OMEGA Photon Collaboration, CERN–PPE/92–135.

[7] H.Clement et al., COSY Proposal No. 30, IKP–KFA 1994.

[8] W.Oelert et al., COSY Proposal No. 11, IKP–KFA 1988.

[9] W.Oelert, Proc. of the 105^{th} WE–Heraeus–Seminar, Bad Honnef, Konferenzen des Forschungszentrums Jülich 12/93 (1993) 127.

[10] R.Maier et al., EPAC 94, Proc. of the Conf. (1994) 165.

[11] L.Jarczyk et al., Annual Report IKP–KFA 1991 (1992) 43.

[12] H.Grote, F.C.Iselin, The MAD Program Version 8.10, CERN/SL/90–13 (AP), CERN, Geneva, Switzerland (1990).

[13] H.Dombrowski, D.Grzonka, W.Hamsink, A.Khoukaz, T.Lister, R.Santo, to be submitted to Nucl. Instr. & Meth.

[14] G.Charpak, Journ. de Phys. 30 (1969) C2–86.

[15] A.H.Walenta et al., Nucl. Instr. & Meth. 92 (1971) 373.

[16] B.Gugulski et al., Report KFA–IKP(I)–1992–3.

[17] Stesalit AG, 4234 Zullwil, Switzerland.

[18] L.Jarczyk et al., Annual Report IKP–KFA 1988 (1989) 152.

[19] M.Sokolowski et al., Annual Report IKP–KFA 1990 (1991) 219.

[20] Bicron Corporation, Newbury, Ohio 44065.

[21] Thorn Emi Electron Tubes Ltd., Ruislip, Middlesex, England.

[22] Hamamatsu Photonics K. K. , Electron Tube Division, 314–5, Shimokanzo, Toyooka-Village, Iwata–gun, Shizuoka–ken, 438.01, Japan.

[23] R.Bröders et al., Annual Report IKP–KFA 1992 (1993) 278.

[24] P.Moskal, Jül–2825 (1993), KFA Jülich.

[25] J.Majewski et al., Annual Report IKP–KFA 1993 (1994) 249.

[26] G.Anton et al., Nucl. Instr. & Meth. A 310 (1991) 631.

[27] M.Wolke, Jül–2852 (1993), KFA Jülich.

[28] ISO/IEC 26.11458 VICbus, Int. Organization for Standardization (1993).

[29] C.F.Parkman, IEEE Trans. Nucl. Sci. , Vol. 39, No. 2 (1992) 77.

[30] D.J.White, Rutherford Appleton Laboratory Report RAL–89–123.

[31] D.J.White, Rutherford Appleton Laboratory Report RAL–90–088.

[32] M.Köhler et al., Jül–3071 (1995), KFA Jülich.

[33] L.Bertolotto et al., Phys. Lett. 345 B (1995) 325.

[34] E.Beuville et al., Nucl. Instr. & Meth. A 288 (1990) 157.

[35] E.Chesi, P.Martinengo, CERN–PS 202 Note (1988).

[36] P.Martinengo, CERN Note (1990).

[37] K.Zwoll et al., IEEE Trans. Nucl. Sci. , Vol. 41, No. 1 (1994) 37.

[38] LeCroy Corporation, Research Systems Division, Chestnut Ridge, New York 10977–6499.

[39] STR330/VIC, Technical Manual, Struck, Hamburg, Germany (1992).

[40] W.Erven et al., IEEE Trans. Nucl. Sci. , Vol. 39, No. 4 (1992) 853.

[41] EUROCOM–6, 68030 CPU Board, Documentation, Eltec elektronik, Mainz, Germany.

[42] FIC 8234 Dual 68040 Fast Intelligent Controller, User's Manual, Creative Electronic Systems, Geneva, Switzerland (1992).

[43] EXB–8500 Cartridge Tape Subsystem, User's Manual, EXABYTE Corporation, Boulder, Colorado (1990).

[44] H.G.Essels et al., GOOSY VME System Description, GSI, Gesellschaft für Schwerionenforschung Darmstadt, Germany (1992).

[45] ISO9506 – Manufacturing Message Specification, Int. Organization for Standardization (1990).

[46] K.H.Watzlawik et al., Annual Report IKP–KFA 1994 (1995) 255.

[47] O.Couet et al., PAW, Physics Analysis Workstation, CERN Program Library, CERN, Geneva, Switzerland (1995).